Experiments in Fluids (2024) 65:85
https://doi.org/10.1007/s00348-024-03823-y

RESEARCH ARTICLE

The influence of crosswinds and leg positions on cycling aerodynamics

Jiaqi Mao[1] · Peng Zhou[1] · Guangsheng Liu[1] · Siyang Zhong[2] · Xun Huang[3] · Xin Zhang[1]

Received: 7 November 2023 / Revised: 8 March 2024 / Accepted: 6 May 2024 / Published online: 27 May 2024

Abstract

This work investigated the influence of crosswinds and leg positions on the aerodynamics of an articulated cycling mannequin on a track bicycle. Force, wake total pressure and wake velocity measurements were made in a low-speed sports wind tunnel of closed-circuit type. The freestream velocity and wheel speeds were kept at 15 m/s. The crank angle of the mannequin was varied across a pedal cycle. Yaw angles from 0° to 20° were examined. The experimental results reveal that the leg position significantly affects the aerodynamic performance of a cyclist. At high yaw angles, the aerodynamic drag on the cyclist showed noticeable deviations between most leg positions and their 180°-apart pairs. A wake analysis technique effectively captured the influence of leg positions on drag. The total pressure deficit contributes dominantly to the overall drag. The wake pressure contours demonstrate how leg-wheel interaction affects the total pressure distribution and drag under crosswinds. This study offers valuable insights into the flow behavior and drag generation around a cyclist with varying leg positions under crosswinds.

1 Introduction

In elite competitive cycling, the winning margin is usually small between the first and second place. To win the competition, cyclists will seek any possible advantage through various training methods. From the view of energy generation and consumption, two approaches are available for performance enhancement: increasing the overall power output and reducing the total resistance opposing the motion of the system. However, improper management of physiological exercise, such as excessive overload and inadequate recovery, may cause overtraining syndrome (Faria et al. 2005; Meeusen et al. 2013), leading to performance decline. On the other hand, reducing the total resistance opposing the motion can decrease the energy requirement from cyclists (McCole et al. 1990; Lucía et al. 2001). If the power output is kept unchanged, the cyclist can achieve higher speed. Therefore, reducing the total resistance can have a positive impact on the performance of elite cyclists in competitive races.

Aerodynamic drag can account for more than 90% of the total resistance that a cyclist can encounter at a travelling speed greater than 50 km/h (Grappe et al. 1997; Kyle and Weaver 2004; Yi et al. 2022). The ever-increasing significance of understanding cycling aerodynamics is represented by the expansion of work produced within the last ten years (Crouch et al. 2017; Malizia and Blocken 2020, 2021). Multiple engineering approaches have been formulated among teams to reduce the aerodynamic drag, which include: adjusting the position of the cyclist (Defraeye et al. 2010; Giljarhus et al. 2020; Polanco et al. 2020; Wang et al. 2022; Schaffarczyk et al. 2022; Giljarhus et al. 2023), optimizing the geometry of the cycling equipment (Chabroux et al. 2012; Castellini et al. 2020), improving the skinsuit design (Underwood and Jermy 2011; Oggiano et al. 2013; Zheng et al. 2021), and taking specific strategies in drafting or overtaking (Barry et al. 2014; Blocken et al. 2018; Spoelstra et al. 2021; Cantos et al. 2023). The above researches emphasize the importance of understanding fundamental flow physics in enhancing the aerodynamic performance of cyclists.

Many of these investigations have provided significant insights into characterizing the flow physics of the cyclist. Crouch et al. (2014) measured the aerodynamic drag and

✉ Peng Zhou
pengzhou@ust.hk

[1] Department of Mechanical and Aerospace Engineering, The Hong Kong University of Science and Technology, Clear Water Bay, Kowloon, Hong Kong, People's Republic of China

[2] Department of Aeronautical and Aviation Engineering, The Hong Kong Polytechnic University, Hung Hom, Kowloon, Hong Kong, People's Republic of China

[3] Department of Aeronautics and Astronautics, College of Engineering, Peking University, Beijing, People's Republic of China

wake of a stationary articulated mannequin with legs positioned around a 360° pedal cycle. Two flow regimes were identified: the wake-symmetric low-drag and wake-asymmetric high-drag regimes. The trailing streamwise vortex pair was suggested as the primary mechanism affecting the change in drag throughout a pedal cycle. Terra et al. (2020) studied the Reynolds number effect over a fixed-leg cycling mannequin based on velocimetry measurements. The near-surface velocity field around the arm and leg confirmed the recirculation regions bounded by two shear layers. The width and length of reverse flow were dependent on the freestream velocity. Critical velocities were concluded upon different bluff body segments to achieve minimum drag. However, most of the studies have only analysed the case of the cyclist aligned with the incoming flow. Researchers have given insufficient attention to the impact of yawed flow on cycling aerodynamics. For road cycling, the yawed inflow typically results from natural crosswinds, which occur regularly in reality and become crucial for cyclist safety (Schepers and Wolt 2012). Cooper (2003) reported that road cyclists typically travel at yaw angles below 16° during 90% of their time on the road. In a velodrome, the yaw inflow arises when the cyclist turns the bicycle on the corner, creating an angle between the incoming wind and travelling direction. Fitzgerald et al. (2019) conducted a field measurement using a bicycle-mounted Cobra probe and observed a yaw angle of up to 8°, compared from the theoretical value of 1.7° based on the cornering theory. The yawed inflow induced by crosswinds is the focus in this work.

Previous experimental studies primarily focused on force measurements at multiple yaw angles to investigate how crosswinds influence the aerodynamic drag of a cyclist. Fintelman et al. (2014) studied the aerodynamic loads on a mannequin with varying torso angles at the yaw angle of up to 90°. The torso angle was found to have a negligible influence on the side force. Fitzgerald et al. (2020) measured the flow angle in front of an instrumented track bicycle with a pedaling mannequin yawed from −15° to 15°. The front disk wheel intensified the measured yaw angle, indicating that in future studies on crosswinds, the choice of the front wheel will affect the incoming flow to the cyclist and the aerodynamic load measured on the system. Clanet et al. (2021) extended the measurement of aerodynamic loads on a real pedalling cyclist to a yaw angle of 180°, which covers the range from headwind to tailwind limits. An simplified analytical expression was derived for the total aerodynamic power by considering the influence of crosswinds.

The crosswinds effect on a single cyclist was also studied via the numerical simulations. Fintelman et al. (2015) performed Reynolds-averaged Navier–Stokes simulation (RANS) on the flow around a road bicycle with a static mannequin at yaw angles ranging from 0° to 90°. The computed force results presented that at small yaw angles (0°), the mannequin predominantly influenced the aerodynamic loads on the system. At large yaw angles (60°), the bicycle turned out to have the dominant contribution.

Despite previous research efforts, there are still gaps in our understanding of cycling aerodynamics under crosswinds. First, the aerodynamic drag was measured either on a pedalling cyclist or a fixed-leg mannequin. The former method simulated the realistic condition and focused on the mean aerodynamic drag throughout a pedal cycle. Its drawback on the repeatability of cycling position makes the flow field measurement difficult to be performed. To solve this problem, the cycling mannequin is used in this work to maintain the position with better repeatability. However, measurements on a fixed-leg mannequin failed to completely depict the aerodynamic drag profile on the cyclist throughout a full pedal cycle. A mannequin with pedalling capability is required to document the drag variation with leg position under crosswinds. The change in drag may be different from the observation at the condition of aligned incoming flow. The pedalling motion can be studied via the steady or unsteady approaches. As Crouch et al. (2016) observed, at the elite-level cycling speed and pedalling frequency, there is only minor variation in the instantaneous aerodynamic drag between a pedalling mannequin and a static mannequin in the same leg position. Therefore, the steady measurement on a cycling mannequin is a good approximation of realistic condition in aerodynamic studies. Second, to the authors' knowledge, there is no experimental measurement of the flow field around a yawed cyclist. Investigating the wake flow is worthwhile to better understand the cyclist aerodynamics under crosswinds. The wake measurement can help identify the change in local drag distribution affected by crosswinds and leg positions.

In this study, the influence of crosswinds and leg positions on the cyclist aerodynamics is studied through wind tunnel experiments. The remaining parts of the paper are organized as follows: Section 2 introduces the experimental configuration; Section 3 presents the measured aerodynamic forces at different yaw angles and leg positions and the associated wake measurements; and Sect. 4 gives the summary.

2 Description of experimental methods

2.1 The HKUST sports wind tunnel

The experiments were conducted in a low-speed sports wind tunnel in Aerodynamics and Acoustics Facility (AAF) at The Hong Kong University of Science and Technology (HKUST) (Yi et al. 2020, 2022). The tunnel is a closed-circuit type with a test section of cross-sectional area of $2.5 \times 2.0\,m^2$ and length of 14.0 m. The flow speed can vary from 5 to 40 m/s, and the inflow turbulence intensity is lower

than 0.12% within the operational speed range. All measurements were conducted at a freestream velocity U_∞ of 15 m/s, a typical speed for competitive track cycling.

2.2 Articulated cycling mannequin model

An articulated cycling mannequin model is used to achieve good repeatability of cycling position in the wind tunnel studies. The mannequin consists of the internal machined metallic skeleton and the external body shell manufactured by Fused Deposition Modeling (FDM) using Acrylonitrile Butadiene Styrene (ABS) material based on a 3D scan of an elite cyclist in sprint position. A 0.5 mm-thick tight-suit was stretched over the external body shell to mitigate the surface roughness caused by FDM and smooth out the discontinuities between body segments. A smooth surface treatment was applied on the uncovered hands and head. The articulated design enables the cyclist geometry and leg positions to be varied for independent investigations. Variation of the leg position is achieved by adjusting the crank angle θ, as indicated in Fig. 1. The crank angle is manually altered to meet the required value aided by an inclinometer, which has a nominal accuracy of ±0.2°. After the crank angle adjustment, the articulation inside the mannequin is locked. The mannequin wears a skinsuit in Lycra material with an average thickness of 0.5 mm. The roughness and stitching pattern of the fabric were characterized over an evaluation area of 1.40 mm × 1.06 mm by a laser confocal microscope, as shown in Fig. 2. The arithmetic mean height S_a (ISO 25178-2 2021) is adopted to present the surface roughness: $S_a = \frac{1}{S_F}\iint_{S_F} |z(m,n)|\, dm\, dn$, where S_F is the evaluation area and $z(m, n)$ stands for the signed normal distance from the fabric surface to the averaged surface at the coordinate of (m, n). The S_a value of the skinsuit has a mean and standard deviation of 0.022 ± 0.0021 mm. No specific patterns were applied to the skinsuit since fabric dependence is not the focus of this study. The helmet and shoes are typical among elite cyclists in professional events. The mannequin was installed on a commercially available LOOK R96 track bicycle frame equipped with a front Corima five-spoke wheel and a rear Corima disk wheel.

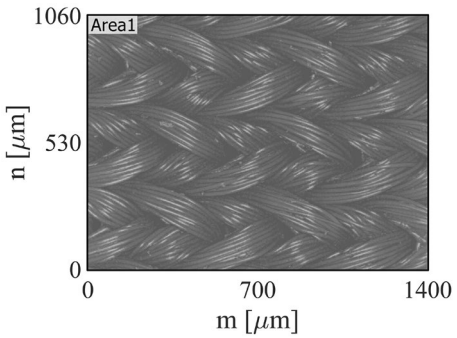

Fig. 2 Stitching pattern of the Lycra material

2.3 Cycling aerodynamic test rig

A cycling aerodynamic test rig is installed on a turntable underneath the wind tunnel floor for force measurements and mechanical support, as presented in Fig. 3. Both wheels rest on respective rollers driven by two individual servo motors. The peripheral speed of both wheels matches the freestream velocity. Loads are measured using a six-component force balance with the measurement accuracy within ±0.2 N for drag force under 80 N. The data acquisition system is based on a National Instrument PXIe-4339 card.

Time-averaged force measurements were made at a 15° interval of crank angle throughout a complete pedal cycle. The sampling frequency and duration for each force measurement were 2000 Hz and 30 s, respectively. The mean value of three separate measurements was taken as the result

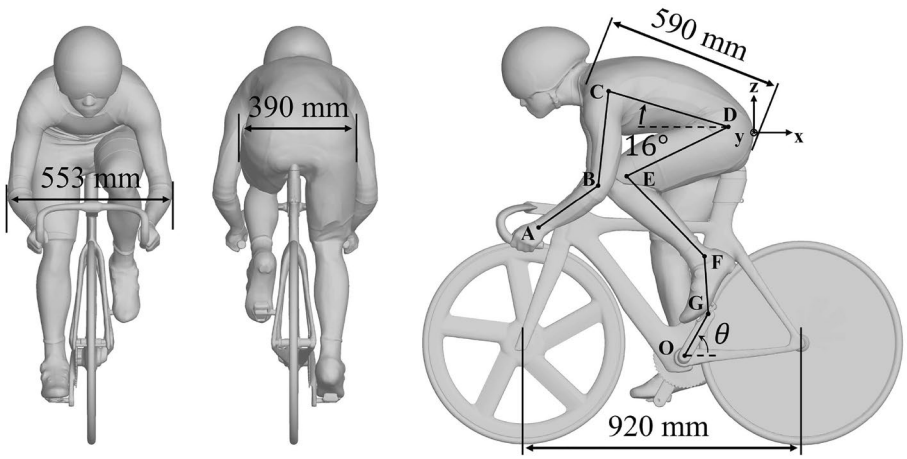

Fig. 1 Geometry of the mannequin and bicycle with key anthropometric parameters

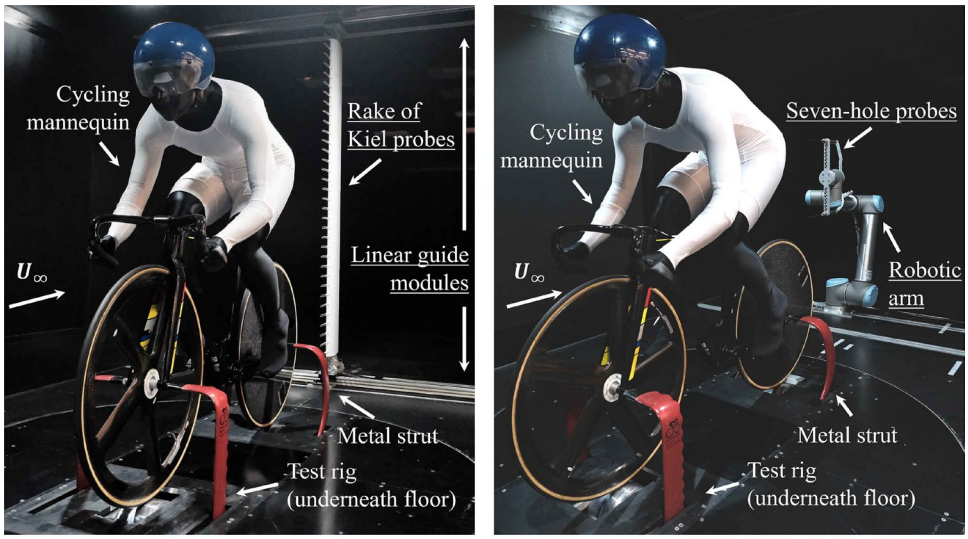

Fig. 3 Schematic of wind tunnel experiment for aerodynamic force and pressure measurements using **a** a rake of Kiel probes and **b** two seven-hole probes

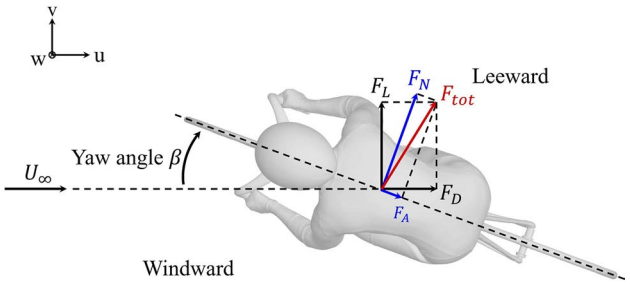

Fig. 4 Illustration of flow angles and definition of forces in the wind-axis and body-axis coordinates

of aerodynamic forces at each leg position and presented with a 95% confidence interval.

Metal struts at the front and rear wheel axles connect the mannequin and bicycle to the force balance underneath the wind tunnel floor. The streamlined struts are yawed with the mannequin and bicycle. The vertical struts are positioned 0.21 m away from the bicycle to reduce their impact on the flow around the test setup. Considering this relatively large distance and the streamlined geometry, the interference effect on the aerodynamic measurement caused by the strut is relatively minor compared to the impact of leg positions. Wind-off measurements were conducted before and after each force measurement to correct for any force drift. The aerodynamic forces on isolated struts were also measured under the same wind speed. Tare and loads on the struts were taken to obtain final aerodynamic loads on the yawed mannequin.

Force results can be described in the body-axis and wind-axis coordinates, as shown in Fig. 4. In the body-axis coordinate, the axial force F_A, opposing the forward motion of cyclist, is defined along the longitudinal centreline of the mannequin, and the normal force F_N is defined perpendicular to the axial force. For the wind-axis coordinate, the aerodynamic forces aligned and perpendicular to the freestream direction are the drag F_D and lift F_L, respectively. The relationship between them is described by the following equations:

$$F_L = F_N \cos\beta - F_A \sin\beta, \tag{1}$$

$$F_D = F_N \sin\beta + F_A \cos\beta. \tag{2}$$

The turntable simultaneously rotates the test rig and the mannequin to control the yaw angle. Thus, the raw force measurements from the balance are in the body-axis coordinate. In the experiments, the yaw angles of the oncoming flow for investigation are 0°, 10°, 16° and 20°. Zero yaw angle is a typical real-world condition that cyclists often encounter in races. Yaw angles beyond 0° are chosen for two reasons: 1) yaw angles from 10° to 20° represent the range in which wind conditions can have a noticeable impact on the aerodynamic performance of cyclists; 2) this range still has a non-negligible probability that cyclist may experience in reality (Barry 2018).

2.4 Total pressure measurements

A rake of Kiel probes was used to measure the total pressure in the wake behind the mannequin. The Kiel probe's shroud acts to straighten the oncoming flow and remove measurement errors associated with varying flow angles. The Kiel probe employed in the study can accurately measure the total pressure for flow with pitch and yaw angles of up to ±45°.

In the tests, a rake of 34 Kiel probes with a spacing of 0.05 m was installed on two belt-driven linear guide

modules. Referring to the rearmost point on the mannequin at zero yaw, where the origin of coordinate is located in Fig. 1, the rake was placed 0.9 m behind the mannequin with a lateral traverse range of ±0.85 m from the wind tunnel centreline and a vertical traverse range of 0.19 m from the wind tunnel floor to a height of 1.84 m. The measurement plane is chosen perpendicular to the freestream direction for all the yaw angles examined. This choice is supported by the numerical study of Fintelman et al. (2015) who identified that at the 15° yaw angle, the dominant flow structures were discovered mainly in the direction of the freestream flow. The total pressure readings were collected at a sampling frequency of 1000 Hz using a Surrey 64-channel pressure scanner system. The array traversed at 23 mm/s after multiple values were evaluated to determine the fastest speed so that the results would not be adversely affected.

Total pressure measurements were conducted for 24 crank angles at all 4 yaw angles. The rake of Kiel probes was a source of blockage behind the mannequin. To evaluate its blockage effect on the cycling aerodynamics, separate force measurements on the mannequin were conducted without the rake installed across all the figurations. The result demonstrated an averaged offset in the $C_D S_D$ of $0.002 \pm 0.0003\,\mathrm{m}^2$, which is within 1% of the $C_D S_D$ of the mannequin. The total pressure coefficient, C_{pt}, is used to demonstrate the wake result, which is defined as:

$$C_{pt} = \frac{P_{t,w} - P_{s,\infty}}{q_c}, \tag{3}$$

where $P_{s,\infty}$ is the static pressure of the undisturbed freestream referenced at the inlet of the test section.

The total pressure coefficient C_{pt} is decomposed into a slowly-varying deterministic component $\overline{C_{pt}}$, and a residual turbulent component C'_{pt} using a Gaussian-weighted moving average filter. A window length of 1000 data points is implemented in the filter, equivalent to 1 s in time domain and a spatial distance of 23 mm in the lateral direction. The window length has been chosen such that the main features of the wake represented by low-frequency peaks and troughs are retained and converged, and the residual component has a near-zero mean, as recommended by Holmes et al. (2008). The captured low-frequency peaks and troughs are linked with the key wake structures. The mean of residual is examined by varying the window length among the tested yaw angles, as demonstrated in Fig. 5. $\overline{C'_{pt}}$ starts to rise from zero at the window length of 1000 data points for all yaw angles. The square of the residual component, $C'_{pt}C'_{pt}$, is used to indicate the turbulence level in the wake (Bell et al. 2016, 2017; Li et al. 2021). The same Gaussian-weighted moving average filter is applied to get the slow-varying component $\overline{C'_{pt}C'_{pt}}$. The constant window length is applied to data sampled by all the Kiel probes among the tested yaw angles and leg positions.

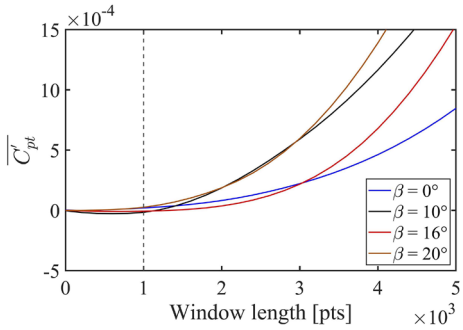

Fig. 5 Variation of $\overline{C'_{pt}}$ with window length in the Gaussian-weighted moving average filter (Data are from the Kiel probe located 0.74 m above the wind tunnel floor. The mannequin is at 90° leg position.)

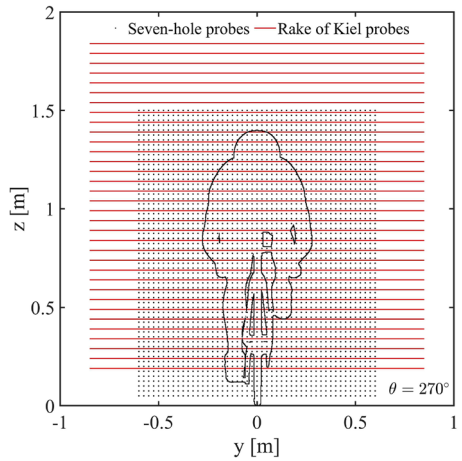

Fig. 6 Schematic of the total pressure and velocity measurement grids behind the mannequin

2.5 Wake velocity measurements

Wake velocity measurements were conducted using a robotic arm and two seven-hole probes, as presented in Fig. 3b. The robotic arm has a positional repeatability of ±0.05 mm. The two probes were installed with a vertical spacing of 0.4 m.

The investigated plane is at the same streamwise location where the total pressure was sampled using the rake of Kiel probes. The plane covers a lateral traverse span of ±0.6 m from the wind tunnel centreline and a vertical traverse span of 0.05 m from the wind tunnel floor to a height of 1.50 m. The measurement locations are uniformly distributed in

vertical and horizontal directions with a spacing interval of 0.025 m, as illustrated in Fig. 6. Calibration data from the probe manufacturer are used to convert the seven sampled pressures to three velocity components. The pressure probes capture the flow within ±45° and have a sensor accuracy of ±1 Pa. The sampling frequency and time are 1000 Hz and 10 s, respectively. Considering the overall scope of this study, wake velocity measurements were only conducted at 4 scenarios: $\theta = 195°, 270°$ at $\beta = 0°$ and $\theta = 90°, 270°$ at $\beta = 20°$.

2.6 Blockage correction in force measurements

The frontal area of the mannequin and bicycle at multiple yaw angles and leg positions is computed to evaluate the blockage effect and facilitate the analysis of force measurements. The computation is based on the 3D scans of the mannequin in various leg positions while mounted on the bicycle. The 3D scanner has an accuracy of up to 0.1 mm, leading to the uncertainty in frontal area calculation of 0.0015 m^2. The blockage ratio of the mannequin and bicycle ranges from 12% to 16% depending on the yaw angle and crank angle. At a constant yaw angle, the frontal area varies within 2% of the mean frontal area over the complete pedal cycle. The correction method in this study is detailed by Maskell (1963). The blockage-corrected dynamic pressure is given by:

$$q_c = q_\infty \left(1 + \epsilon \frac{C_{D,uncorr} S_D}{C}\right), \tag{4}$$

where q_∞ is the dynamic pressure of the undisturbed stream, ϵ is an empirical blockage factor, and it usually approximates to 5/2 for three-dimensional flow, $C_{D,uncorr}$ is the uncorrected drag coefficient, S_D is the frontal area of the mannequin and bicycle in the wind-axis coordinate and C is the cross-sectional area of the test section. In the remaining text, the force results are represented by the corrected force area $C_i S_i = F_i / q_c$ or the corrected force coefficient $C_i = F_i / q_c S_i$ where $i = L, D, N, A$ stands for terms linked to the lift, drag, normal force and axial force, respectively; S_L is the lateral area of the model in the wind-axis coordinate; S_N and S_A represent the lateral and frontal areas of the model in the body-axis coordinate, respectively.

3 Results and discussion

3.1 Effect of yaw angles and leg positions on aerodynamic loads

The 360° pedal cycle can be divided into two halves based on the leg position: the first half cycle is 0°–180° and the second half is 180°–360°. At 0° yaw, the axial force varies by 15% throughout a full pedal cycle. Figure 7 presents the time-averaged axial force area versus crank angle for the tested yaw angles. Both halves of the pedal cycle have almost identical axial force profiles. Minor disagreement (2%) between some leg positions and their 180°-apart pairs may be attributed to the model asymmetry. As Fig. 7b indicated, the identity in $C_A S_A$ between two halves of the pedal cycle generally applies at 10° yaw. However, a maximum distinction of 8% is discovered between leg positions in the range of $15° \leq \theta \leq 75°$ and their 180°-apart pairs. A drop in $C_A S_A$ is observed at 210° leg position, followed by a gradual increase. The decrease and subsequent recovering in $C_A S_A$ become more evident and obvious at 16° yaw and 20° yaw. Corresponding leg position shifts to 225° and 240°.

When the yaw angle reaches 16°, the symmetry in $C_A S_A$ observed at 0° and 10° yaw is no longer valid. The lowest $C_A S_A$ is found at 225° leg position, and the maximum $C_A S_A$ occurs at 285° leg position. At 20° yaw, $C_A S_A$ is almost independent of the leg position within two ranges: 0°–30° and 90°-165°. $C_A S_A$ of the second half cycle is generally lower than the value of the first half over the first 60° rotation of leg position.

A common feature of $C_A S_A$ profile is recognized at 16° and 20° yaw. Starting from the first 75° rotation of leg position, $C_A S_A$ of the second half cycle constantly surpasses the value in the first half. At large yaw angles, elevating the windward leg higher and further ahead results in a markedly reduced axial force compared to the action of lifting the leeward leg in a similar manner. The maximum reduction between the two halves is around 6% and 12% at 16° and 20° yaw, respectively. The constant difference of the axial force area infers that under large crosswinds, locating the raised leg windward can reduce the aerodynamic resistance experienced by the cyclist.

The change in $C_A S_A$ with leg position can be explained by the variation in frontal area, axial force coefficient, or a combination of both. After the frontal area is extracted, the variation in C_A with leg position is presented in Fig. 8. The small fluctuation in frontal area across different leg positions makes C_A the major factor in affecting $C_A S_A$.

According to the force diagram in Fig. 4, both the change in lift and drag can contribute to the large variation of the axial force between one leg position and its 180°-apart pair. Their relationship can be described by the following equation:

$$\Delta(C_A S_A) = \Delta(C_D S_D \cos\beta) + \Delta(C_L S_L \sin\beta), \tag{5}$$

where:

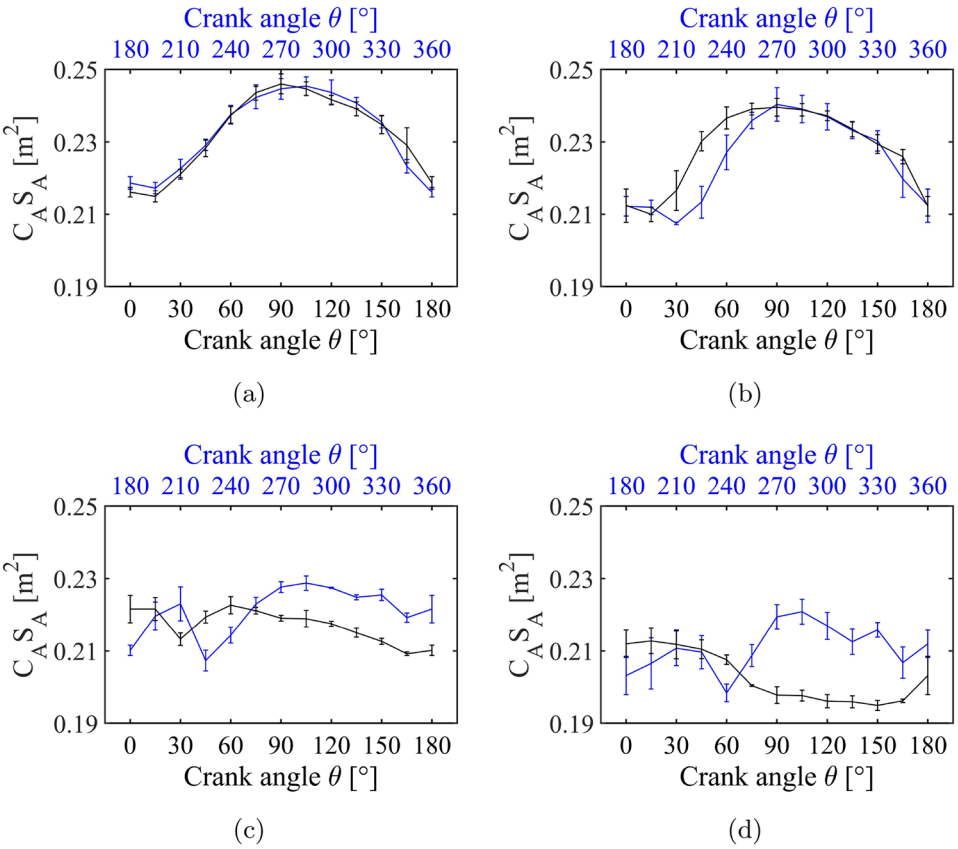

Fig. 7 Axial force area of the mannequin in the two halves of pedal cycle: **a** $\beta = 0°$; **b** $\beta = 10°$; **c** $\beta = 16°$; **d** $\beta = 20°$

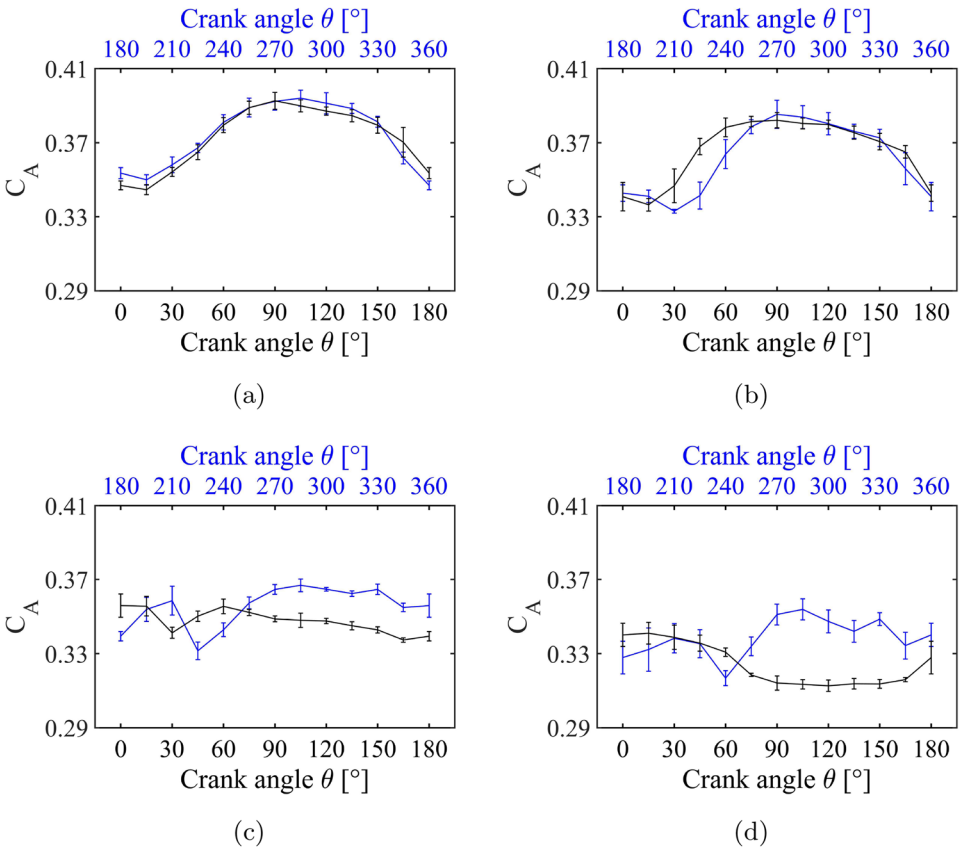

Fig. 8 Axial force coefficient of the mannequin in the two halves of pedal cycle: **a** $\beta = 0°$; **b** $\beta = 10°$; **c** $\beta = 16°$; **d** $\beta = 20°$

$$\Delta(C_A S_A) = (C_A S_A)_\theta - (C_A S_A)_{\theta+180^\circ},$$
$$\Delta(C_D S_D \cos\beta) = (C_D S_D \cos\beta)_\theta - (C_D S_D \cos\beta)_{\theta+180^\circ},$$
$$\Delta(C_L S_L \sin\beta) = (C_L S_L \sin\beta)_{\theta+180^\circ} - (C_L S_L \sin\beta)_\theta \text{ with } \theta \in [0^\circ, 180^\circ].$$

The individual contribution of lift and drag to the axial force is presented in Fig. 9. At 10° yaw, the deviation in $C_A S_A$ is caused by the combined efforts from the change in lift and drag. However, at 16° and 20° yaw, the variation in drag becomes the dominant reason for the deviation in $C_A S_A$, while the change in lift is negligible.

The drag measurements are also presented since its variation dominates the change in $C_A S_A$ under large yaw angles. The drag area increases with the yaw angle at most leg positions. As shown by Fig. 10, at increasing yaw angles, the drag area demonstrates less fluctuation with the leg position compared with the result at 0° yaw (15% at 0°; 11% at 10°; 6% at 16° and 20°). The frontal area fluctuates less than 2% across all the leg positions at these yaw angles, making itself not the primary contribution to the change in drag area. Thus, as presented in Fig. 11, the drag coefficient is the dominant variable to explain the drag behavior of the yawed mannequin, which will be justified by the total pressure measured in the wake.

3.2 Drag coefficient estimation via wake integral approach

The wake measurements are first used to find the source of drag and relate the drag with flow field. The momentum integral equation is applied to a control volume surrounding the mannequin. This work computed the drag coefficient using data from the entire measurement plane with the area of S_W. Referring to previous studies on road vehicles (Van Dam 1999; Urquhart et al. 2018), the time-averaged drag coefficient can be expressed in terms of total pressure deficit $\overline{C_{D_{pt}}}$, longitudinal velocity deficit $\overline{C_{D_u}}$, and crossflow deficit $\overline{C_{D_\Omega}}$:

$$C_{D_{wake}} = \iint_{S_W} \overline{C_{D_{pt}}} - \overline{C_{D_u}} + \overline{C_{D_\Omega}}\, dy\, dz = \iint_{S_W} \left(\frac{P_{t,\infty} - P_{t,w}}{q_\infty S}\right) - \frac{1}{S}\left(1 - \frac{u}{U_\infty}\right)^2 + \left(\frac{v^2 + w^2}{U_\infty^2 S}\right) dy\, dz, \tag{6}$$

where S_W is the area of the wake measurement plane (Kiel probe: $S_W = 1.7\,\text{m} \times 1.65\,\text{m}$; Seven-hole probe: $S_W = 1.45\,\text{m} \times 1.2\,\text{m}$), $P_{t,\infty}$ is the total pressure of the undisturbed freestream; $P_{t,w}$ is the local total pressure in the wake behind the mannequin; u, v, w are the three components of the velocity. When the rake of Kiel probes is applied, the longitudinal velocity and crossflow deficit are ignored in the integration. The total pressure deficit reflects the energy loss in the wake, which will be influenced by the crosswinds and leg positions. Understanding the distribution of total

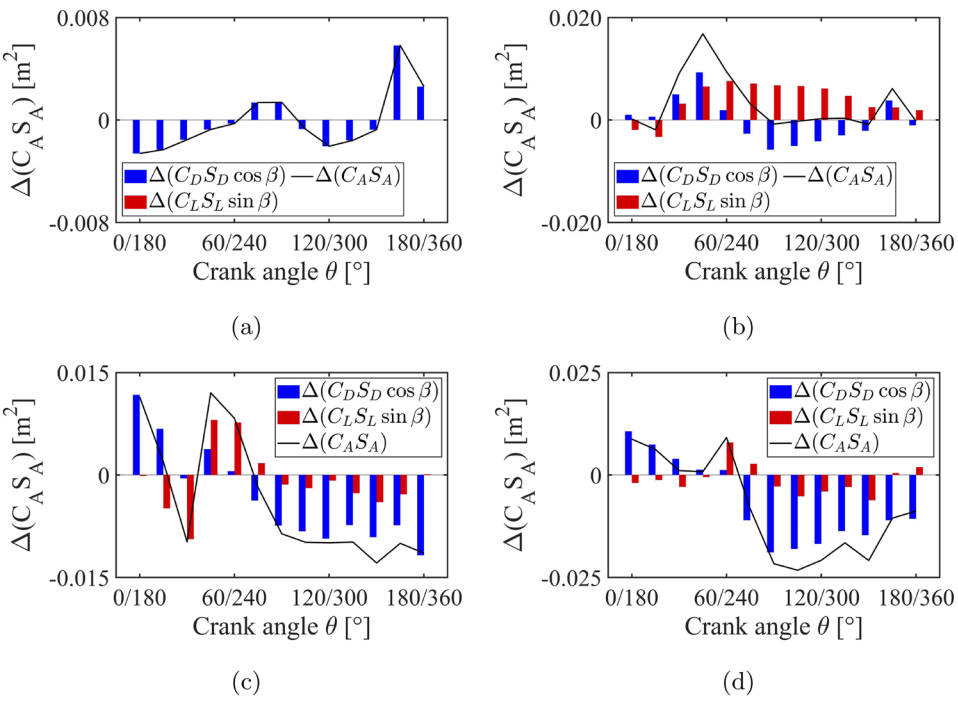

Fig. 9 Variation of the contribution from lift, drag to the axial force on the mannequin between two halves of pedal cycle: **a** $\beta = 0°$; **b** $\beta = 10°$; **c** $\beta = 16°$; **d** $\beta = 20°$

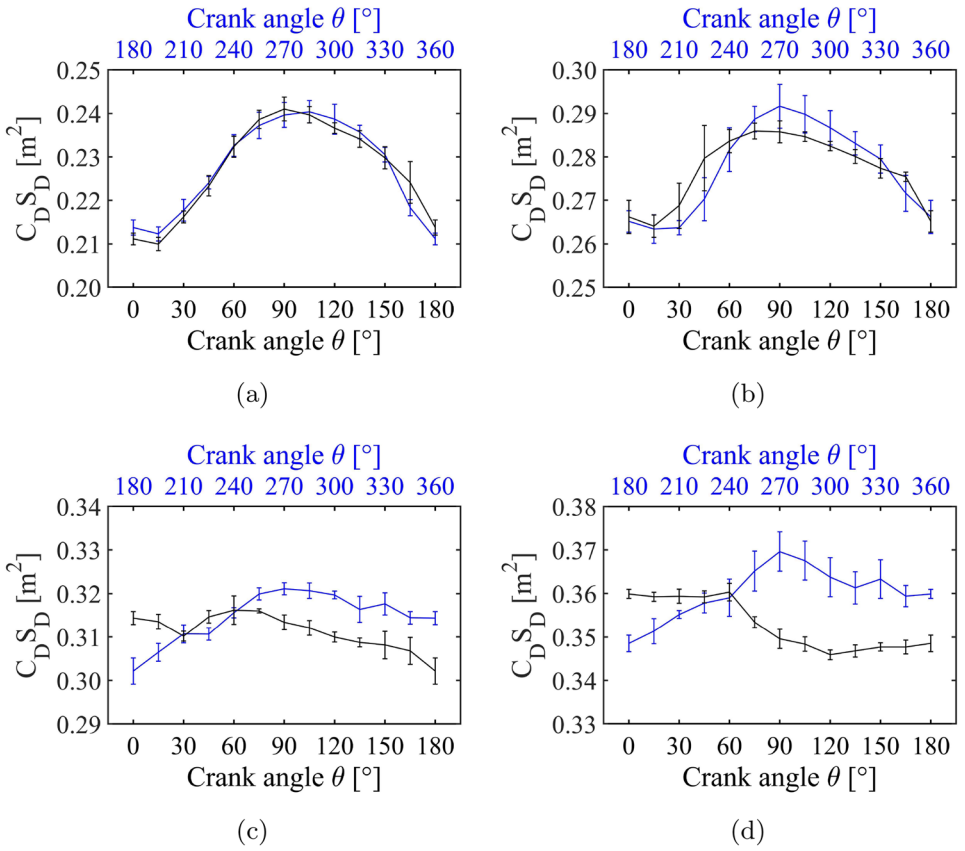

Fig. 10 Drag area of the mannequin in the two halves of pedal cycle: **a** $\beta = 0°$; **b** $\beta = 10°$; **c** $\beta = 16°$; **d** $\beta = 20°$

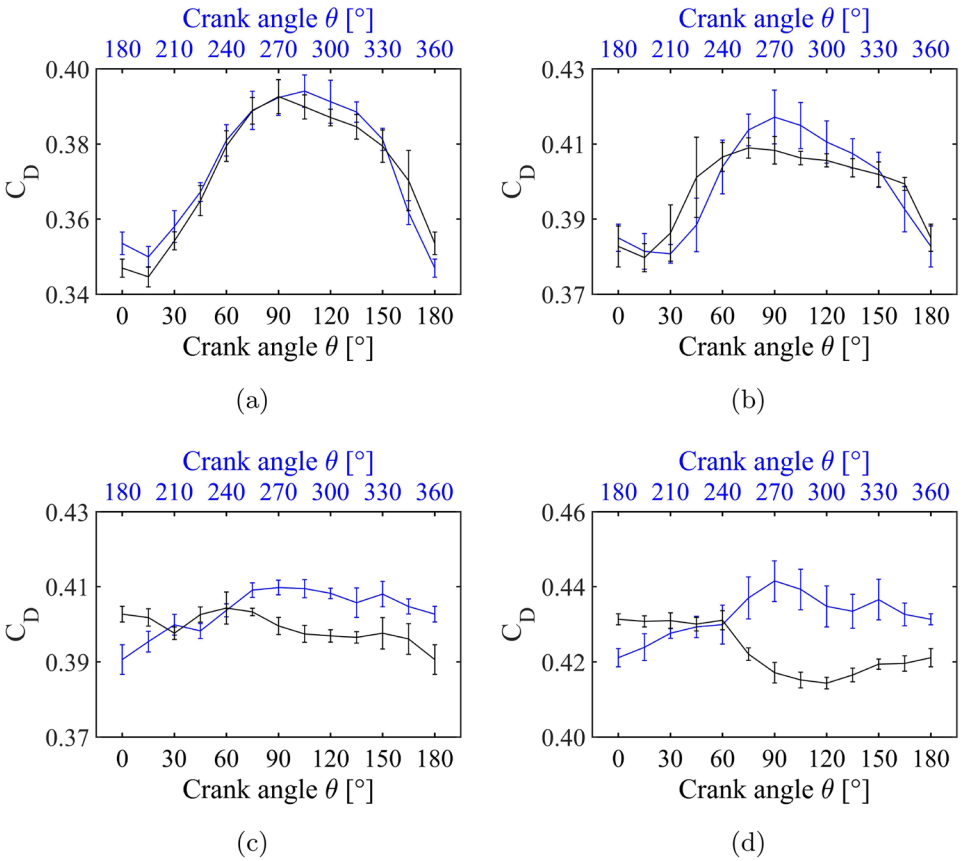

Fig. 11 Drag coefficient of the mannequin in the two halves of pedal cycle: **a** $\beta = 0°$; **b** $\beta = 10°$; **c** $\beta = 16°$; **d** $\beta = 20°$

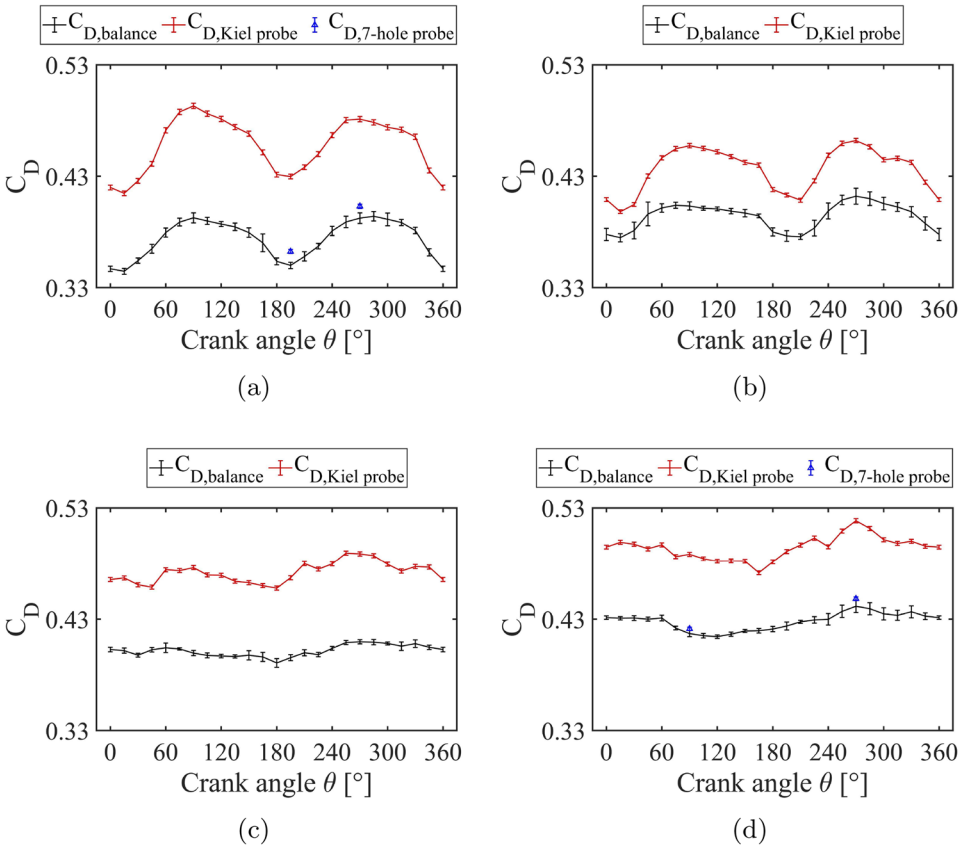

Fig. 12 Drag coefficient of the mannequin obtained via wake integration and force balance over a complete pedal cycle: **a** $\beta = 0°$; **b** $\beta = 10°$; **c** $\beta = 16°$; **d** $\beta = 20°$

pressure is useful in locating the origin of aerodynamic drag on cyclists. To assess the significance of the ignored terms in the overall drag estimation, additional three-component wake velocities were measured for representative configurations. Figure 12 compares the drag coefficient obtained via the wake integral approach and force balance measurement.

The wake integral method based on the Kiel probes reaches good qualitative agreement in the trend of drag variation with leg positions by only considering the total pressure deficit. Integrating the drag from the total pressure only will overestimate the value. The difference between the measured and estimated drag coefficients depends on the yaw angle but is almost irrelevant to the leg position. At these four configurations, where all the local drag terms are included for drag estimation, the integrated drag coefficients agree well with the force balance data. The integration of each time-averaged term in Eq. 6 is listed in Table 1. Across the selected configurations, the longitudinal velocity and crossflow deficit make relatively minor contributions to the overall drag compared with the total pressure deficit.

The wake integral analysis is furthered at 0° yaw to determine the source of drag in terms of total pressure deficit. As presented in Fig. 14a, the individual contribution of the leg and right legs of the mannequin to its drag is evaluated by focusing on the left and right portions of the measurement plane separately. Recent studies (Crouch et al. 2014; Zheng et al. 2024) on the evolution of flow patterns behind the cyclist suggest that the time-averaged wake structures typically evolve in the streamwise direction as they propagate downstream, with the intensity diminishing. Figure 13a and b shows the distributions of the streamwise vorticity Ω_x and turbulence intensity I_{uvw} behind the mannequin, which are defined as:

Table 1 Comparison of integrated drag coefficient with the value measured using the force balance

β	θ	C_D	$C_{D,\text{7-hole probe}}$	$\iint_{S_W} \overline{C_{D_{pt}}}\, dy\, dz$	$\iint_{S_W} \overline{C_{D_u}}\, dy\, dz$	$\iint_{S_W} \overline{C_{D_\Omega}}\, dy\, dz$
0°	195°	0.3499	0.3624	0.4229	0.0710	0.0105
0°	270°	0.3924	0.4031	0.4952	0.1083	0.0161
20°	90°	0.4171	0.4214	0.5331	0.1513	0.0395
20°	270°	0.4415	0.4483	0.5545	0.1437	0.0375

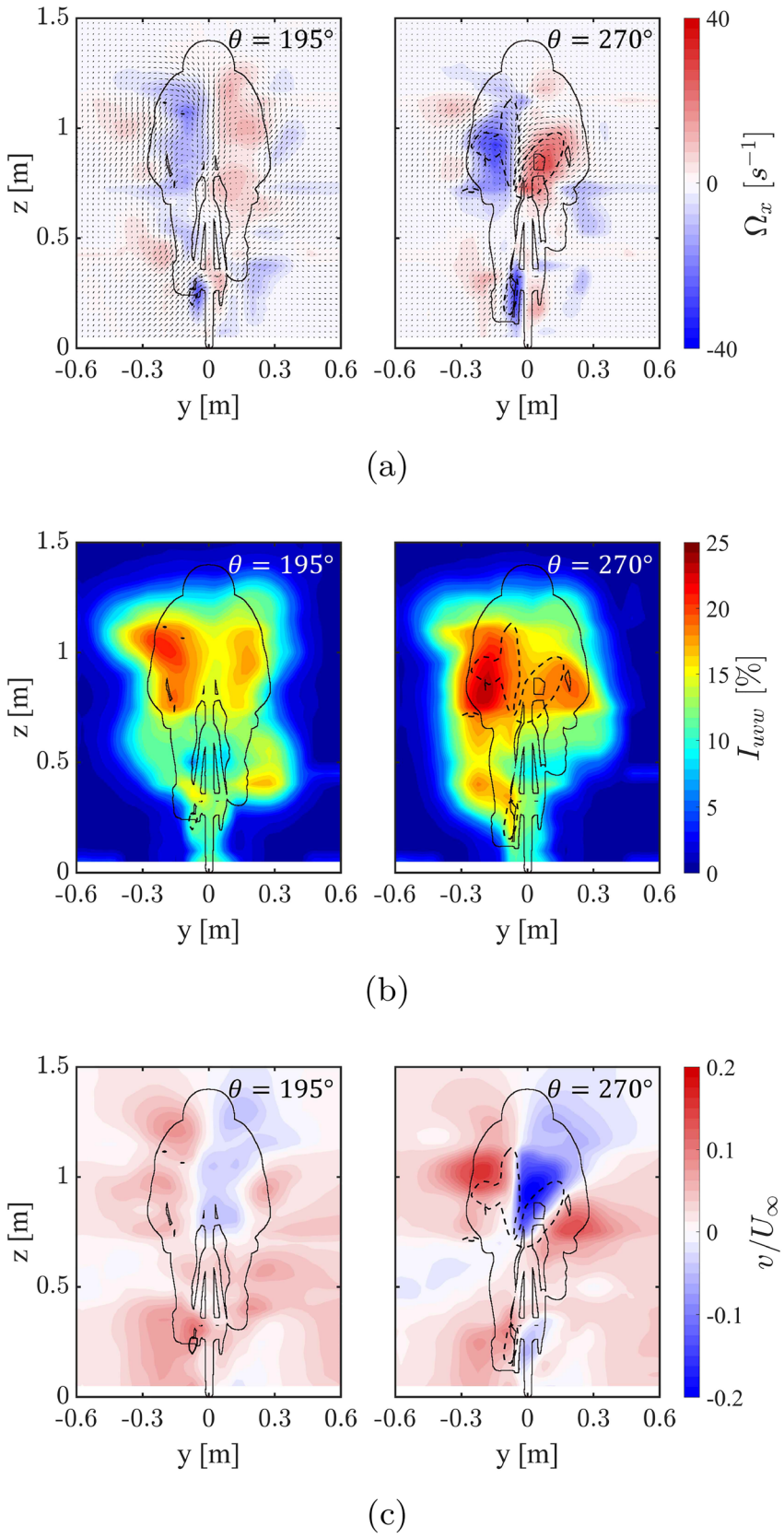

Fig. 13 Contours of the time-averaged **a** streamwise vorticity Ω_x, **b** turbulence intensity I_{uvw} and **c** normalized lateral velocity v/U_∞ for $\theta = 195°$ and 270° at $\beta = 0°$ with the mannequin and bicycle overlaid for reference [Vortex structures are outlined using dashed black line by the Q-criterion (Q=300) in this work

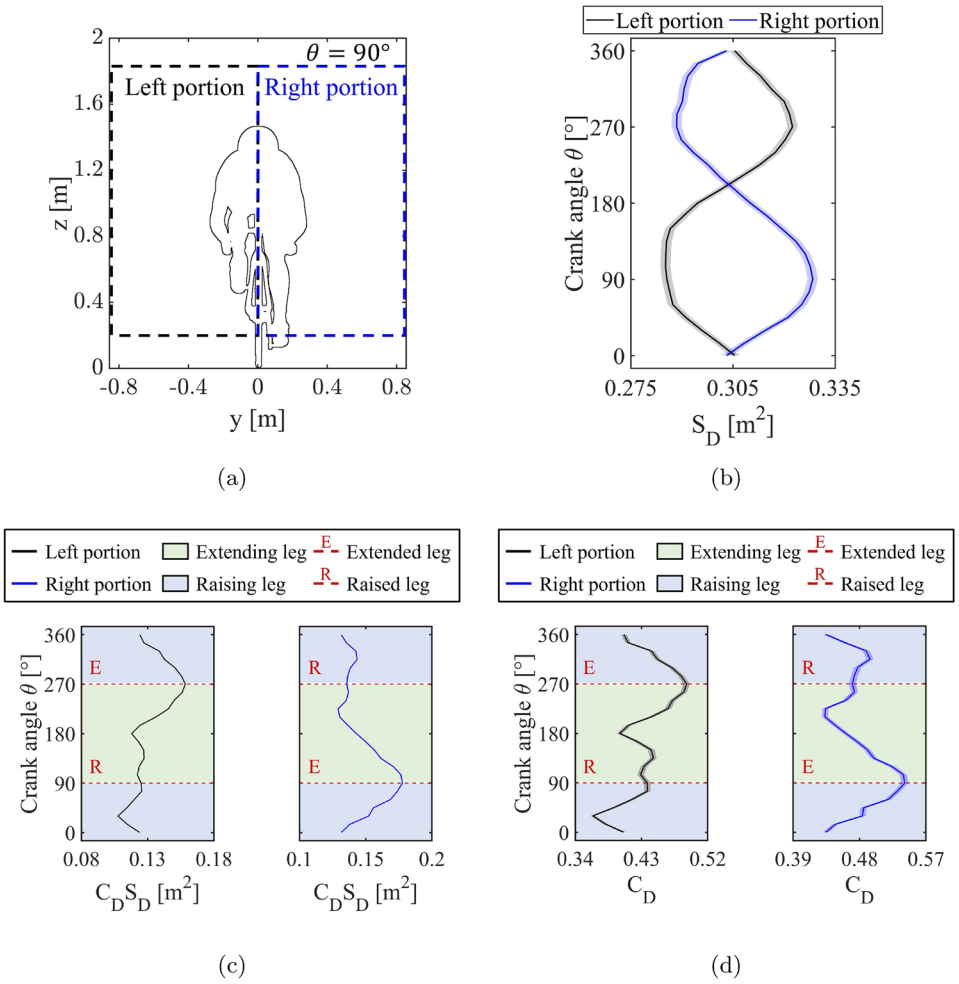

Fig. 14 **a** Schematic of the left and right portion in the measurement plane for frontal area and drag calculation at $\beta = 0°$; Variation of the **b** frontal area; **c** drag area and **d** drag coefficient with leg positions in the left and right portion

$$\Omega_x = \frac{1}{2}\left(\frac{\partial w}{\partial y} - \frac{\partial v}{\partial z}\right), \tag{7}$$

$$I_{uvw} = \frac{\sqrt{1/3(\sigma_x{}^2 + \sigma_y{}^2 + \sigma_z{}^2)}}{U_\infty} \times 100\%, \tag{8}$$

where $\sigma_j (j = x, y, z)$ is the root-mean-square of the velocity fluctuations in the streamwise, lateral and vertical direction, respectively. The streamwise vorticity and turbulence intensity exhibit approximately symmetric distributions around the centre plane at $\theta = 195°$. A counter-rotating vortex pair is captured at the leg position of 270°, as the dominant flow structure. It is noteworthy that when the leg position switches from 195° to 270°, the left extending leg results in a wider wake and higher I_{uvw} compared with the right raising leg. This change in leg position significantly impacts the flow structures behind the mannequin, with the effects predominantly propagating in the streamwise direction downstream from the corresponding leg.

The contours of normalized lateral velocity for $\theta = 195°$ and 270° are demonstrated in Fig. 13c. The positive v/U_∞ on the left side indicates the wake deflection toward the centre axis of the mannequin, where a clear boundary of $v/U_\infty \sim 0$ can be distinguished. The positive v/U_∞ on the right side shows a strong traverse flow from the raised leg. In short, the behaviour of v/U_∞ demonstrates that at the current streamwise location, the flow originating from the left and right leg is converging toward the centre axis of the mannequin. The left and right portions of the wake generally correspond to the left and right leg, respectively.

The integrated drag area in the left and right portions is shown in Fig. 14c. The extended leg contributes dominantly to the drag area in a complete pedal cycle. Moving the raised leg lower and forward leads to a generally stable drag area until its linked crank is horizontally positioned. Further moving the leg toward the extended position will dramatically increase the drag area. In the raising period of the leg, its drag area drops continuously until its linked crank tilts

upwards by 30°. Advancing the raising motion more slightly increases the integrated drag area.

Varying leg position leads to frontal area change in the left and right portions, as indicated in Fig. 14b. The extended leg has a frontal area 14% larger than the raised leg. The drag coefficient is then extracted to exclude the influence of frontal area in the left and right portions, as demonstrated in Fig. 14d. The extended leg still makes the highest drag coefficient. However, a comparable contribution from the raised leg to the drag coefficient is observed. When the leg is crossing its raised position, the resultant variation of drag coefficient is more pronounced compared with the change in drag area. The analysis indicates that (1) the extended leg causes more drag compared with the raised leg; (2) the extended and raised leg contributes comparably to the drag coefficient of the mannequin. Since the raised leg has a smaller frontal area, its contribution to the drag shrinks.

3.3 Flow structures in the wake

Force result indicates that under large yaw angles, the axial force and drag coefficients of the mannequin no longer follow similar patterns in the first and second half of the pedal cycle. Locating the raised leg windward can effectively reduce the drag coefficient within a specific range of leg positions, which depends on the yaw angle.

To investigate the reason for the drag behavior, detailed total pressure field measurements in the wake behind the mannequin are presented in a range of leg positions at four different yaw angles. The contours of $\overline{C_{pt}}$ and $\sqrt{\overline{C'_{pt}C'_{pt}}}$ are presented in Figs. 15 and 16. Four leg positions (15°, 90°, 195° and 270°) are chosen for discussion due to two reasons: 1) at 0° and 10° yaw, these four leg positions correspond to local extrema in the force profile indicating the diverse flow behaviours; 2) the mannequin experiences greatest contrast in external geometry when switching between these leg positions.

3.3.1 Wake flow structures at 0° yaw

At 0° yaw, $\overline{C_{pt}}$ distribution in the wake is approximately symmetric in the low-drag leg position (15°, 195°). The upper half of the wake is governed by two separate regions of considerable pressure deficit. It is likely caused by the flow separation from the side torso, which is indicated by high pressure fluctuation in these regions. The low-pressure region extends toward the middle portion of the wake at the height $z \in [0.5\,\text{m}, 1\,\text{m}]$. The middle low-pressure region has a relatively reduced pressure fluctuation. It is likely caused by the symmetric flow from both sides of the bicycle which maintains a stable flow pattern and reduces the pressure fluctuation.

At the high-drag position (90°, 270°), the mannequin has one leg extended and another raised, leading to an asymmetric projected region. The low-pressure region caused by the flow separation from the side torso is also observed on the extended leg side, where a more intense pressure fluctuation is discovered. On the raised leg side, the flow remains largely attached over the side torso and fore portion of the upper leg, leading to a high streamwise velocity reaching the flow separation point (Crouch et al. 2014). The flow separates on the rear portion of the raised leg, which causes a larger velocity deficit. Therefore, minimum $\overline{C_{pt}}$ is observed behind the raised leg.

The lower half of the wake also contains two low-pressure regions on the two sides of the mannequin at the low-drag position. They may attribute to the flow separation from the lower leg. When the mannequin is in high-drag position, the low-pressure regions will either extend vertically in the extended leg side or merge with the wake caused by the flow separation from the rear portion of the upper leg in the raised leg side.

The wake integral analysis considers the dimension and intensity of the low-pressure area. Although the minimum $\overline{C_{pt}}$ concentrates behind the raised leg, the influenced region is small. The flow separation on the extended leg introduces a wider region of a slightly larger $\overline{C_{pt}}$. For the extended leg, its resultant $\overline{C_{pt}}$ cannot overcome the influence of the more expanded wake. Therefore, the extended leg causes more drag compared with the raised leg.

3.3.2 Wake flow structures under crosswinds

When the crosswind is present, the wake of the mannequin is deflected toward windward. One low-pressure region consistently appears at the middle wake area, as indicated by the black dashed rectangle in Fig. 15. Another low-pressure region occurs at the right wake area, which is within the projected arm region, as shown by the red dashed rectangle in Fig. 15. The distribution and intensity of these low-pressure regions vary across different leg positions and yaw angles.

The middle pressure loss attributes to the rear wheel and the left leg that is upstream from the rear wheel. Changing yaw angle varies the level of exposure of rear wheel to the wake from the left leg of the mannequin.

When the leg position is fixed, increasing yaw angle will broaden the low-pressure region and increase the pressure loss. At 0° yaw, the wake from the left leg convects downstream with a minimum flow interaction with the rear wheel. At larger yaw angles, the rear wheel has more exposure to the turbulent wake from the left leg. Especially at 16° and 20° yaw, the location with minimum $\overline{C_{pt}}$ concentrates on

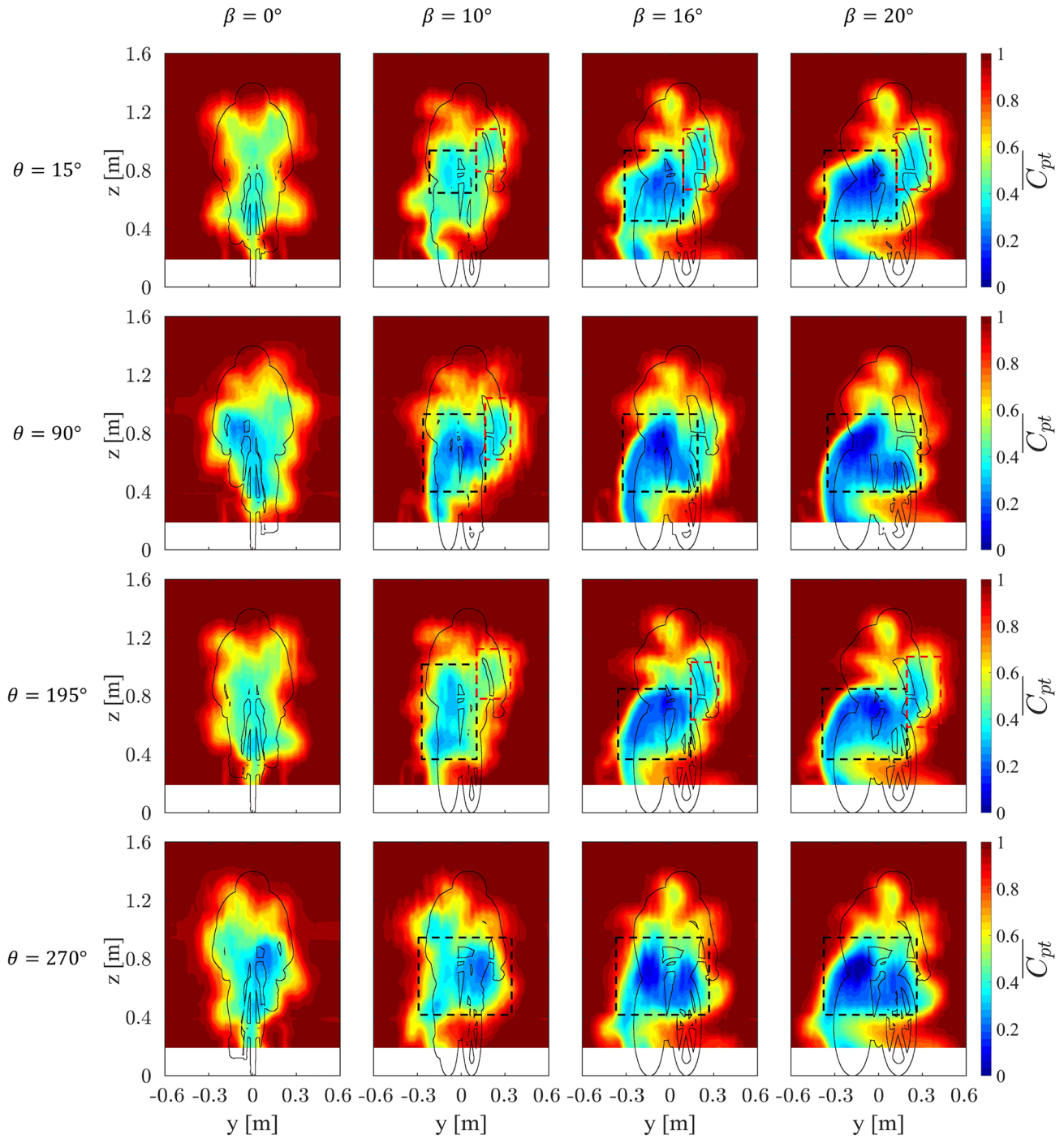

Fig. 15 Contours of the slowly-varying deterministic component in total pressure coefficient, $\overline{C_{pt}}$, at four leg positions for four yaw angles with the mannequin and bicycle overlaid for reference

the projected region where the left leg and rear wheel overlap, which indicates the dominant source of drag at these configurations.

The force measurements at 16° and 20° yaw have shown that switching the leg position from 90° to 270° causes a 6% − 7% increment in drag coefficient. The increase is dominated by the additional pressure deficit due to the flow separation from the raised leg. The raised leg is leeward at 270° leg position, where the pressure deficit in wake contains two valleys of $\overline{C_{pt}}$. The left valley grows in terms of magnitude and size at increasing yaw angle. The right one is generally stable concerning changing yaw

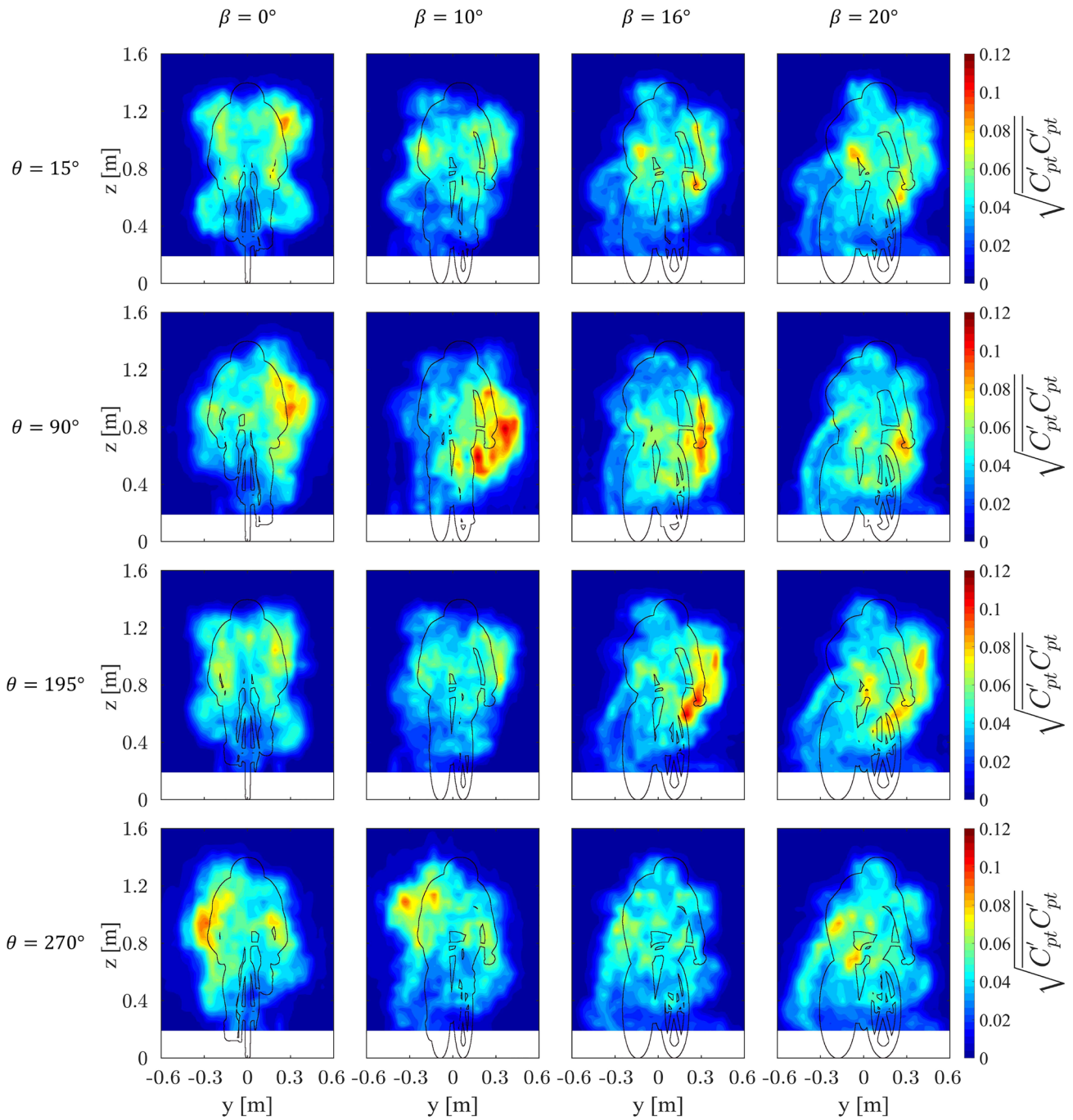

Fig. 16 Contours of the root-mean-square of the residual turbulent component in total pressure coefficient, $\sqrt{\overline{C'_{pt}C'_{pt}}}$, at four leg positions for four yaw angles with the mannequin and bicycle overlaid for reference

angle. Thus, it is attributed to the flow separation from the raised leg only. At 90° leg position, the rear wheel is in the low-velocity wake from the windward raised leg, which reduces the drag on the rear wheel. The region with large pressure loss extends toward the bottom of the measurement plane. The magnitude and size of the region are less influential than the effect of the flow separation from the raised leg.

The effect of leg positions on $\overline{C_{pt}}$ is also influenced by the yaw angle. At 10° yaw, the $\overline{C_{pt}}$ contours show a strong dependence on leg positions. Distinct differences on the distribution and intensity of the low-pressure regions can be

visualized, which can explain a relatively large drag coefficient variation with leg position in Fig. 12b. The 15° and 195° leg position lead to a smaller and weaker low-pressure region, while the 90° and 270° leg position introduce a much larger and more intense pressure deficit region. At 16° and 20° yaw, changing leg position minorly influences the $\overline{C_{pt}}$ contours, which can explain a relatively small drag coefficient fluctuation in Fig. 12c and d.

The right pressure loss may refer to the flow separation from the right arm. This pressure deficit is consistently observed at the leg position of 15° and 195° with its intensity slightly increasing at large yaw angles. A relatively higher level of turbulence can be identified from the $\sqrt{\overline{C'_{pt}C'_{pt}}}$ contours around the projected arm region.

At 90° leg position, this pressure deficit region is first observed at 10° yaw, together with an intense pressure fluctuation. The possible reason is that the right arm locates leeward under crosswinds. Normally, as a feature of the yawed bluff body, the flow separation usually occurs earlier and more forcefully on the leeward, leading to a wider wake with higher turbulence. The continuous drop in turbulence level at 16° and 20° yaw on the 90° leg position may be attributed to the increased separated distance between the arm and torso. At 270° leg position, no obvious pressure deficit is observed in the wake contour around the projected arm region. The intensity of pressure fluctuation drops at increasing yaw angle.

Beyond 10° yaw, a constant pressure loss is detected behind the helmet in the top wake. Its dimension and magnitude are nearly independent of the leg position. The pressure loss may refer to the flow separation from the helmet. The $\sqrt{\overline{C'_{pt}C'_{pt}}}$ contour near the helmet demonstrates that the level of turbulence is greater around the periphery of the low-pressure core.

Further details of flow structures under crosswinds were investigated for the leg position of 90° and 270° at 20° yaw. Figure 17a and b demonstrates the distributions of the streamwise vorticity Ω_x and turbulence intensity I_{uvw}, respectively, behind the mannequin. The low-pressure region identified in the $\overline{C_{pt}}$ contour contains a counter-rotating vortex pair. Switching the leg position from 90° to 270° does not bring about substantial changes in the vorticity distribution. However, it does result in a shift of the region with high I_{uvw} toward windward. As shown in Fig. 17c, the distribution of normalized lateral velocity reveals an inclined boundary with $v/U_\infty \sim 0$, which is different from the wake at 0° yaw where there is a deflection toward the centre axis of the mannequin.

In summary, at 0° yaw, the location of raised leg is the dominant factor leading to the total pressure loss, which affects the drag on the cyclist. Under crosswinds, multiple regions of pressure loss were captured in the wake with their distribution and intensity dependent on the leg positions and yaw angles. The drag increase in the second half of pedal cycle observed at 16° and 20° yaw is attributed to the leeward positioning of the raised leg such that its low-total-pressure wake is unblocked by the rear wheel when convecting downstream. When the raised leg is windward, its wake reaches the rear wheel, which reduces the drag on the rear wheel, leading to a lower drag on the whole system.

4 Summary

In the present work, an experimental investigation of the flow around a full-scale cycling mannequin under steady crosswinds is conducted. The force balance measurements reveal that under crosswinds, the leg position greatly affects the aerodynamic drag and axial force of a cyclist. The investigation of crosswind effect on cycling aerodynamics should consider a full pedal cycle rather than resting solely on a single leg position. Noticeable axial force and drag deviations were captured between specific leg positions and their 180°-apart pairs. The largest difference in axial force can be 12% at 20° yaw. The cyclist is suggested to position the raised leg windward to reduce the aerodynamic drag at 16° and 20° yaw.

The wake-integrated drag coefficient agrees well with the balance measurements across different yaw angles and leg positions in terms of the trend of drag variation with the leg position. Integrating the drag solely from the total pressure would slightly overestimate the value. However, a more accurate agreement with the balance measurements can be achieved when all the local drag terms are included in the wake integral approach. The wake contours demonstrate that the location of the raised leg and the flow interaction between the leg and rear wheel are the key factors affecting the total pressure loss in the wake and the overall drag coefficient of the mannequin under crosswinds. A weak flow interaction occurs at the 0° yaw, so the flow separation from the raised leg majorly causes the pressure loss. At increasing yaw angles, the rear wheel is exposed to the wake from the left leg. The low-velocity wake reaches the rear wheel, leading to a reduced drag on the wheel. With the raised leg leeward, its unaffected wake convects downstream, causing more drag compared with the case of the windward raised leg. The results and discussion provide a more comprehensive understanding of the mechanisms of flow physics and force generation for a yawed mannequin. The study can give more insights into cycling aerodynamics by considering the effect of crosswinds and leg positions.

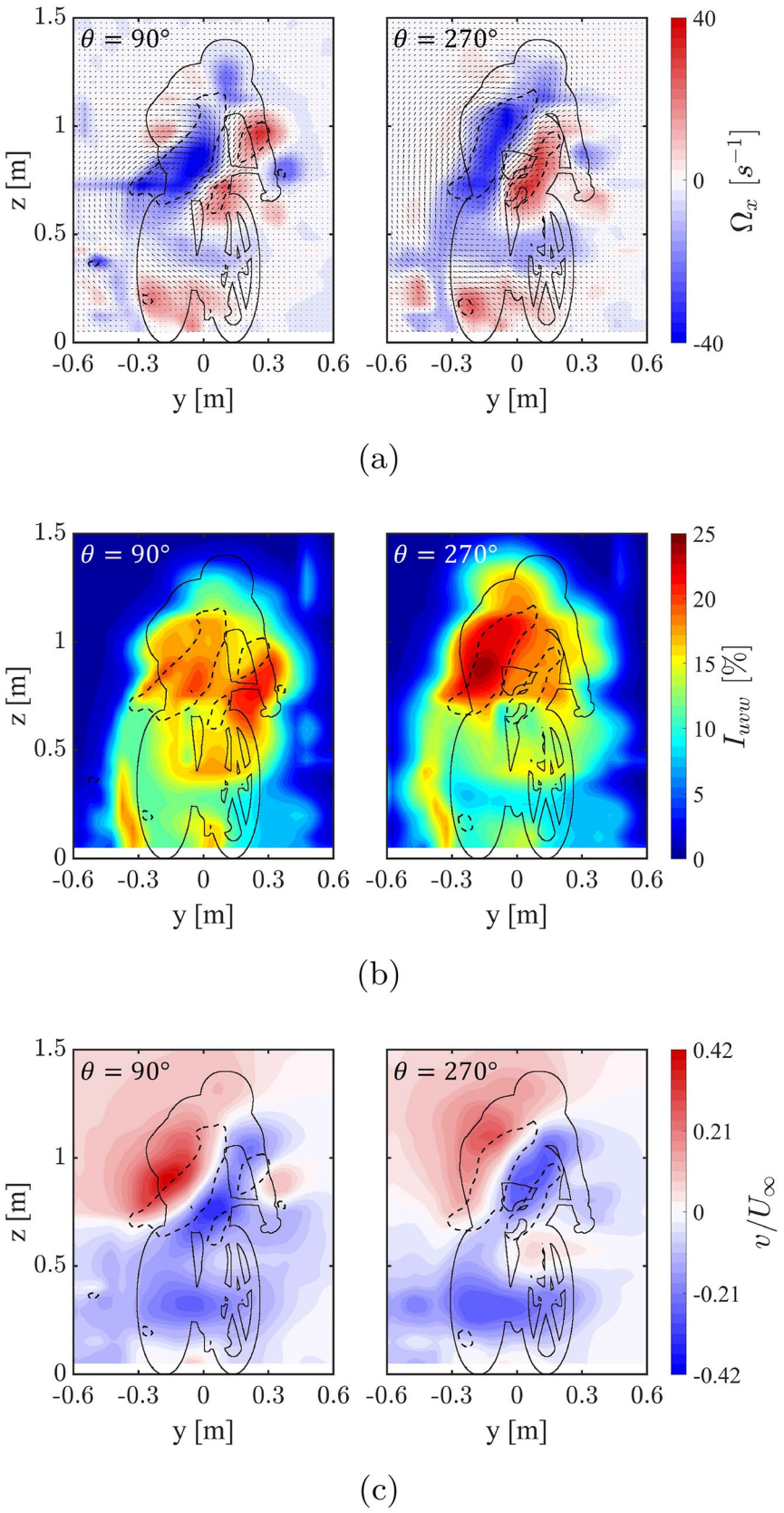

Fig. 17 Contours of the time-averaged **a** streamwise vorticity Ω_x, **b** turbulence intensity I_{uvw} and **c** normalized lateral velocity v/U_∞ for $\theta = 90°$ and 270° at $\beta = 20°$ with the mannequin and bicycle overlaid for reference [Vortex structures are outlined using dashed black line by the Q-criterion (Q=500) in this work.]

Acknowledgements This work is partially supported by the Hong Kong Innovation and Technology Commission (ITC) (No. ITS/354/18FP). This work was performed in Aerodynamics and Acoustics Facility (AAF) (aaf.ust.hk). The authors would like to thank Sam Wong, the AAF technical officer, for his great assistance on the experiment.

Author contributions Jiaqi Mao conducted the experiment and wrote the original manuscript. Peng Zhou and Guangsheng Liu provided experiment support. Peng Zhou, Siyang Zhong, Xun Huang and Xin Zhang contributed to discussions and review. Peng Zhou and Xin Zhang supervised the work.

Funding Open access funding provided by Hong Kong University of Science and Technology. This work is partially supported by the Hong Kong Innovation and Technology Commission (ITC) (No. ITS/354/18FP).

Data availability The data that support the findings of this study are available within the article upon reasonable request.

Declarations

Ethical approval Consent from the cyclist was obtained for scanning, and the protocol was approved by the Human and Artefacts Research Ethics Committee of the Hong Kong University of Science and Technology under HREP-2024-0002

References

Barry N (2018) A new method for analysing the effect of environmental wind on real world aerodynamic performance in cycling. Proceedings 2(6):211

Barry N, Sheridan J, Burton D et al (2014) The effect of spatial position on the aerodynamic interactions between cyclists. Procedia Eng 72(2014):774–779

Bell J, Burton D, Thompson M et al (2016) Dynamics of trailing vortices in the wake of a generic high-speed train. J Fluids Struct 65:238–256

Bell J, Burton D, Thompson M et al (2017) The effect of tail geometry on the slipstream and unsteady wake structure of high-speed trains. Exp Thermal Fluid Sci 83:215–230

Blocken B, van Druenen T, Toparlar Y et al (2018) Aerodynamic drag in cycling pelotons: new insights by CFD simulation and wind tunnel testing. J Wind Eng Ind Aerodyn 179:319–337

Cantos S, Mok KP, Zhou P et al (2023) A numerical study of cyclist-cyclist aerodynamic interaction towards efficient overtaking strategy. J Fluid Eng 146(021202):1–12

Castellini M, Barbanera M, Scungio M et al (2020) Numerical and experimental analysis of turbulent fluid flow around latest generation cycling frame. Int J Comput Meth Exp Measur 8(4):355–366

Chabroux V, Barelle C, Favier D (2012) Aerodynamics of cyclist posture, bicycle and helmet characteristics in time trial stage. J Appl Biomech 28(3):317–323

Clanet C, Abel H, Brunet E et al (2021) Cycling speeds in crosswinds. Phys Rev Fluids 6(124601):1–14

Cooper K (2003) Truck aerodynamics reborn - lessons from the past. SAE Technical Paper, 2003-01-3376 112:132–142

Crouch TN, Burton D, Brown NAT et al (2014) Flow topology in the wake of a cyclist and its effect on aerodynamic drag. J Fluid Mech 748:5–35

Crouch TN, Burton D, Thompson MC et al (2016) Dynamic leg-motion and its effect on the aerodynamic performance of cyclists. J Fluids Struct 65:121–137

Crouch TN, Burton D, LaBry ZA et al (2017) Riding against the wind: a review of competition cycling aerodynamics. Sports Eng 20(2):81–110

Defraeye T, Blocken B, Koninckx E et al (2010) Aerodynamic study of different cyclist positions: CFD analysis and full-scale wind-tunnel tests. J Biomech 43(7):1262–1268

Faria EW, Parker DL, Faria IE (2005) The science of cycling: physiology and training - part 1. Sports Med 35:285–312

Fintelman D, Sterling M, Hemida H et al (2014) The effect of crosswinds on cyclists: an experimental study. Procedia Eng 72:720–725

Fintelman D, Hemida H, Sterling M et al (2015) CFD simulations of the flow around a cyclist subjected to crosswinds. J Wind Eng Ind Aerodyn 144:31–41

Fitzgerald S, Kelso R, Grimshaw P et al (2019) Measurement of the air velocity and turbulence in a simulated track cycling team pursuit race. J Wind Eng Ind Aerodyn 190:322–330

Fitzgerald S, Kelso R, Grimshaw P et al (2020) Observations of the flow experienced by a track cyclist using velodrome, wind tunnel, and potential flow investigations with an instrumented bicycle. J Wind Eng Ind Aerodyn 206(104374):1–12

Giljarhus KET, Stave DÅ, Oggiano L (2020) Investigation of influence of adjustments in cyclist arm position on aerodynamic drag using computational fluid dynamics. Proceedings 49(159):1–6

Giljarhus KET, Liland FF, Oggiano L (2023) Virtual skeleton methodology for athlete posture modification in CFD simulations. Sports Eng 26(39):1–7

Grappe F, Candau R, Belli A et al (1997) Aerodynamic drag in field cycling with special reference to the Obree's position. Ergonomics 40(12):1299–1311

Holmes JD, Hangan HM, Schroeder JL et al (2008) A forensic study of the lubbock-reese downdraft of 2002. Wind Struct 11(2):137–152

ISO 25178–2, (2021) Geometrical product specifications (GPS) - Surface texture: areal - part 2: terms, definitions and surface texture parameters. Standard, International Organization for Standardization, Geneva, Switzerland

Kyle C, Weaver M (2004) Aerodynamics of human-powered vehicles. Proceed Instit Mech Eng: J Power Energy 218(3):141–154

Li XB, Liang XF, Wang Z et al (2021) On the correlation between aerodynamic drag and wake flow for a generic high-speed train. J Wind Eng Ind Aerodyn 215(104698):1–16

Lucía A, Hoyos J, Chicharro JL (2001) Physiology of professional road cycling. Sports Med 31:325–337

Malizia F, Blocken B (2020) Bicycle aerodynamics: history, state-of-the-art and future perspectives. J Wind Eng Ind Aerodyn 200(104134):1–30

Malizia F, Blocken B (2021) Cyclist aerodynamics through time: Better, faster, stronger. J Wind Eng Ind Aerodyn 214(104673):1–33

Maskell E (1963) A theory of the blockage effects on bluff bodies and stalled wings in a closed wind tunnel. Aeronaut Res Council Reprt Memoranda 3400:1–27

McCole S, Claney K, Conte JC et al (1990) Energy expenditure during bicycling. J Appl Physiol 68(2):748–753
Meeusen R, Duclos M, Foster C et al (2013) Prevention, diagnosis and treatment of the overtraining syndrome: joint consensus statement of the European college of sport science (ECSS) and the american college of sports medicine (ACSM). Eur J Sport Sci 13(1):1–24
Oggiano L, Brownlie L, Troynikov O et al (2013) A review on skin suits and sport garment aerodynamics: guidelines and state of the art. Procedia Eng 60(2013):91–98
Polanco AP, Muñoz LE, Doria A et al (2020) Selection of posture for time-trial cycling events. Appl Sci 10(6546):1–19
Schaffarczyk A, Koehn S, Oggiano L et al (2022) Aerodynamic benefits by optimizing cycling posture. Appl Sci 12(8475):1–15
Schepers P, Wolt KK (2012) Single-bicycle crash types and characteristics. Cycling Res Int 2(1):119–135
Spoelstra A, Sciacchitano A, Scarano F et al (2021) On-site drag analysis of drafting cyclists. J Wind Eng Ind Aerodyn 219(104797):1–11
Terra W, Sciacchitano A, Scarano F (2020) Cyclist Reynolds number effects and drag crisis distribution. J Wind Eng Ind Aerodyn 200(104143):1–13
Underwood L, Jermy M (2011) Fabric testing for cycling skinsuits. Procedia Eng 13(2011):350–356
Urquhart M, Sebben S, Sterken L (2018) Numerical analysis of a vehicle wake with tapered rear extensions under yaw conditions. J Wind Eng Ind Aerodyn 179:308–318
Van Dam CP (1999) Recent experience with different methods of drag prediction. Prog Aerosp Sci 35(8):751–798
Wang S, Pitman J, Brown C et al (2022) The influence of the interrelationship of leg position and riding posture on cycling aerodynamics. Fluids 7(18):1–16
Yi W, Morris SY, Zhou P, et al (2020) Aerodynamic measurements of a single wheel in ground effect. AIAA Paper 2020-2784
Yi W, Bertin C, Zhou P et al (2022) Aerodynamics of isolated cycling wheels using wind tunnel tests and computational fluid dynamics. J Wind Eng Ind Aerodyn 228(105085):1–12
Zheng C, Zhou P, Zhong S et al (2021) An experimental investigation of drag and noise reduction from a circular cylinder using longitudinal grooves. Phys Fluids 33(115110):1–11
Zheng C, Zhou P, Mao X et al (2024) On the evolution of flow structures around a track cyclist. Phys Fluids 36(015160):1–14